Probing the Source of the Interfacial Dzyaloshinskii-Moriya Interaction Responsible for the Topological Hall Effect in Metal/Tm_{3}Fe_{5}O_{12} Systems

Aidan J. Lee, Adam S. Ahmed, Jose Flores, Side Guo, Binbin Wang, Nuria Bagués, David W. McComb, and Fengyuan Yang

Phys. Rev. Lett. **124**, 107201 — Published 9 March 2020

DOI: 10.1103/PhysRevLett.124.107201

Probing the Source of Interfacial Dzyaloshinskii-Moriya interaction Responsible for Topological Hall Effect in Metal/$Tm_3Fe_5O_{12}$ Systems

Aidan J. Lee[1], Adam S. Ahmed[1], Jose Flores[1], Side Guo[1], Binbin Wang[2,3], Nuria Bagués[3], David W. McComb[2,3], and Fengyuan Yang[1]

[1]Department of Physics, The Ohio State University, Columbus, OH, USA

[2]Department of Materials Science and Engineering, The Ohio State University, Columbus, OH, USA

[3]Center for Electron Microscopy and Analysis, The Ohio State University, Columbus, OH, USA

Abstract

Interfacial Dzyaloshinskii-Moriya interaction (DMI) is responsible for the emergence of topological spin textures such as skyrmions in layered structures based on metallic and insulating ferromagnetic films. However, there is active debate on where the interfacial DMI resides in magnetic insulator systems. We investigate the topological Hall effect, which is an indication of spin textures, in $Tm_3Fe_5O_{12}$ films capped with various metals. The results reveal that Pt, W, and Au induce strong interfacial DMI and topological Hall effect, while Ta and Ti cannot. This study also provides insights into the mechanism of electrical detection of spin textures in magnetic insulator heterostructures.

Magnetic skyrmions are attractive for memory applications due to their nanoscale sizes, robust topological protection, and low energy for manipulation.[1-10] Most efforts in the skyrmion field have focused on metallic ferromagnetic (FM) systems with bulk or interfacial Dzyaloshinskii-Moriya interaction (DMI), while FM insulators (FMI) are much less explored. Meanwhile, skyrmions in heavy-metal (HM)/FMI bilayers offer high crystal quality, low density of defects, and low magnetic damping. Recently, signatures of topological spin textures in Pt/$Tm_3Fe_5O_{12}$ (TmIG) bilayers have been detected by the topological Hall effect (THE),[11, 12] where a spin current is generated in the HM via the spin Hall effect (SHE) and used to detect the FMI magnetization[13, 14] and topological spin textures such as skyrmions. However, there are debates in the field on whether the main source of interfacial DMI stems from the HM/FMI interface[11, 12] or the FMI/substrate interface,[15-17] as well as the mechanism for electrical detection of magnetic textures in HM/FMI bilayers.[11] Recent work on TmIG and $Y_3Fe_5O_{12}$ films with minimum thicknesses of 5 nm were studied using domain wall and spin wave propagation, which found that either the majority of DMI was generated at the FMI/substrate interface or changing the capping layer did not affect the strength of the DMI.[15-17]

Previously,[12] we reported the observation of topological Hall effect in Pt/TmIG bilayers within certain temperature (T) regions tunable by the TmIG thickness, which was termed the spin-Hall topological Hall effect (SH-THE). In this letter, we aim to uncover the source of the interfacial DMI and the mechanism for the SH-THE detection of spin textures through a systematic study of TmIG films capped with various metal films and bilayers. Our results rule out the magnetic proximity effect as the origin for topological spin textures and demonstrate that a HM must be in direct contact with the TmIG film in order to detect a non-zero topological Hall effect. This indicates that the interfacial DMI responsible for the emergence of skyrmions arises

from the HM/TmIG interface rather than the TmIG/substrate interface.

Epitaxial TmIG(2 nm) films are grown by off-axis sputtering[18] on substituted-$Gd_3Ga_5O_{12}$ (sGGG) substrates at a temperature of 700°C. The TmIG thin films exhibit high crystalline quality with perpendicular magnetic anisotropy and no magnetic dead layer (as an example, 1.85 nm TmIG films remain ferrimagnetically ordered at room temperature).[12] The TmIG films are cooled to room temperature before the deposition of metal layers including Pt, W, Ta, Au, and Ti. Figure 1a shows a cross-sectional scanning transmission electron microscopy (STEM) image of a Pt/TmIG/sGGG(111) sample viewed along the $[11\bar{2}]$ direction taken by an aberration corrected FEI Titan 60/300 STEM at 300 kV. Because the atomic numbers of Tm (Z = 69) and Fe (Z = 26) are close to those of Gd (Z = 64) and Ga (Z = 31), and there are no detectable defects near their interface, it is difficult to discern TmIG from the substrate. To identify the TmIG/sGGG interface, Fig. 1b shows an energy dispersive X-ray (EDX) color map of Ga in sGGG, Tm in TmIG, and Pt on top, revealing their interfaces. Finally, the films are patterned into 400 μm × 100 μm Hall bars using a standard photolithography procedure and ion milling. Figures 1c show an atomic force microscopy (AFM) image of a 5 μm × 5 μm region on the Hall bar of a Ta(3 nm)/TmIG(2 nm) bilayer on sGGG(111) with a root-mean-square roughness of 0.29 nm.

The Hall measurements are carried out in a flow cryostat and an oven inside an electromagnet with a maximum field (H) of 16 kOe. Figure 1d shows a schematic of the measurement setup superimposed over an optical image of a Hall bar. A positive and negative direct current (DC) of 300 μA is applied to the Hall bar, resulting in current densities ranging from 7.5×10^8 to 1.5×10^9 A/m^2 depending on the thickness of the metal layer.

Figure 2 shows the Hall resistivity for HM/TmIG bilayers with Pt, W, Ta, and Au with a

varying degree of interfacial DMI and spin Hall angle. The measured Hall resistivity includes, $\rho_{xy} = \rho_{\mathrm{OHE}} + \rho_{\mathrm{SH-AHE}} + \rho_{\mathrm{SH-THE}}$, where ρ_{OHE}, $\rho_{\mathrm{SH-AHE}}$, and $\rho_{\mathrm{SH-THE}}$ are due to the ordinary Hall effect (OHE) which is proportional to H, the spin-Hall anomalous Hall effect (SH-AHE) proportional to the out-of-plane magnetization of TmIG, and the SH-THE proportional to the density of topological spin textures, respecctively.[12] It has been demonstrated that a significant topological Hall effect is observed in Pt/TmIG bilayers in various temperature windows depending on the TmIG thickness.[11, 12] Figure 2a shows the Hall resistivity for a Pt(3 nm)/TmIG(2 nm) bilayer at 340 K with the linear OHE background subtracted, which exhibits saturation at large magnetic fields due to the SH-AHE and clear peaks at lower magnetic fields due to the SH-THE.

We extend this study to other heavy metals to gain deeper insights. Figure 2b shows the result for a W(2 nm)/TmIG(2 nm) bilayer at 300 K, which is similar to the Pt/TmIG bilayer with a larger SH-THE signal in a lower temperature region. Therefore, W can also supply sufficient interfacial DMI to generate a topological Hall effect that strongly points towards the stabilization of topological spin textures. However, the Ta(3 nm)/TmIG(2 nm) bilayer exhibits a qualitatively different behavior as shown in Fig. 2c. Within the temperature range of 250-450 K, the Ta/TmIG bilayer only shows a slanted '*S*'-shaped Hall curve due to the SH-AHE with a linear OHE background. This indicates that Ta can measure the TmIG magnetization through the SH-AHE, but cannot induce topological spin textures, for which the reason is unclear considering the similarities between W and Ta. Note that the sign of the SH-AHE is the same for all three metals, and is unaffected by the opposite sign of spin Hall angles ($\theta_{\mathrm{SH}} > 0$ for Pt and $\theta_{\mathrm{SH}} < 0$ for W and Ta).[19] This is consistent with experiments and theoretical predications which demonstrate[20] that the sign of SH-AHE is a function of $(\theta_{\mathrm{SH}})^2$. Lastly, Fig. 2d shows the Hall

resistivity for an Au(2 nm)/TmIG(2 nm) bilayer, where only the linear OHE is present.

The fact that the Au/TmIG bilayer only exhibits the OHE provides the opportunity to use Au as a spacer layer to investigate the origin of the SH-THE. There has been debate in the field about whether the detected Hall peaks originate from the magnetic proximity effect in Pt/TmIG bilayers.[11] To address this issue, we decouple Pt from TmIG using a Pt(3 nm)/Au(1 nm)/TmIG(2 nm) trilayer. In this trilayer, Pt generates the spin accumulation at the Pt/Au interface via the SHE, which diffuses to the Au(1 nm)/TmIG interface with little decay given the spin diffusion length (λ_{sf}) of ~30 nm in Au.[21] The spins then exert a spin-orbit torque on the TmIG moment at the interface, generating voltage signals in the longitudinal (spin Hall magnetoresistance) and transverse direction (SH-AHE and/or possibly SH-THE).[13]

As a heavy metal, Au can potentially induce a sizable interfacial DMI at the Au/TmIG interface and generate a topological Hall effect. This is confirmed in Fig. 3a where prominent SH-THE peaks are observed for the Pt/Au(1 nm)/TmIG trilayer at 350 K. Together, Figs. 2d and 3a offer several key insights. First, Au induces strong interfacial DMI on TmIG, similar to Pt and W. Second, Au alone cannot detect either the magnetization (via SH-AHE) or spin textures (SH-THE) in TmIG despite its comparable spin Hall angle as Ta.[19] One possible reason for this behavior is that the large spin diffusion length[22] of Au suppresses the spin accumulation at the Au/TmIG interface, which hinders the SH-AHE or SH-THE detection. Meanwhile, the Pt/Au(1 nm) can detect the TmIG moment where Pt is the spin generator/detector and Au is transparent to spins. Third, the magnetic proximity effect is not the origin of the detected THE because the Au spacer prevents Pt from getting magnetized by proximity. The observation of the same THE signals between the Pt/TmIG bilayer and the Pt/Au/TmIG trilayer proves that the THE resistivities originate from the SH-THE scheme.

To extract $\rho_{\mathrm{SH-THE}}$, the SH-AHE contribution which is proportional to the TmIG magnetization needs to be subtracted. The magnetization of the 2 nm TmIG films is too small to be accurately measured. Therefore, we approximate it as $\tanh(H/H_0)$ where H_0 is a fitting parameter as shown in Fig. 3a.[12] Figure 3b shows $\rho_{\mathrm{SH-THE}}$ after the subtraction of $\rho_{\mathrm{SH-AHE}}$ with a THE field range of ±2 kG and a peak of 5.8 nΩ cm.

To verify if the interfacial DMI comes from the metal/TmIG interface, we choose a lighter element, Ti, as the spacer in a Pt(3 nm)/Ti(1 nm)/TmIG(2 nm) trilayer, where Ti ($\lambda_{sf} \sim$ 13 nm) is transparent for spins.[23] Figure 3c shows that only the OHE and SH-AHE are detected for the Pt(3 nm)/Ti(1 nm)/TmIG(2 nm) trilayer at 325 K (and all other temperatures measured), indicating that 1) the Ti layer is transparent to spins generated in Pt allowing spins to interact with TmIG, and 2) the Ti/TmIG interface has small interfacial DMI which does not induce a topological Hall effect. The distinct results of Au and Ti spacers in the trilayers suggest that Au with large spin-orbit coupling can generate sufficient interfacial DMI to stabilize spin textures in TmIG, while Ti with small spin-orbit coupling cannot. The presence of SH-AHE in both Pt/Au/TmIG and Pt/Ti/TmIG trilayers, but SH-THE only in Pt/Au/TmIG indicates that the interfacial DMI stems from the metal/TmIG interface rather than the TmIG/sGGG interface. If the interfacial DMI was induced at the TmIG/sGGG interface, the SH-THE signals would be present regardless of the spacer layer.

Interestingly, Ta generates a sufficient spin accumulation such that the SH-AHE can be detected, but the Ta/TmIG interface does not harbor a strong enough interfacial DMI to produce a topological Hall effect, as shown in Fig. 2c. To confirm this understanding, we measure a Pt(3 nm)/Ta(1 nm)/TmIG(2 nm) trilayer as shown in Fig. 3d, which exhibits only the SH-AHE at 293 K (and all temperatures), demonstrating that the Ta/TmIG interface does not stabilize topological

spin textures.

Using the procedure discussed above,[12] we extract the SH-THE resistivities and construct the *H*-*T* phase diagrams for two bilayers and two trilayers. Figure 4a shows the phase diagram for the Pt(3 nm)/TmIG(2 nm) bilayer within a temperature window of 310-400 K. The W(2 nm)/TmIG(2 nm) bilayer in Fig. 4b exhibits a qualitatively similar behavior except that $\rho_{\mathrm{SH-THE}}$ shifts to a lower temperature region at 260-370 K. Furthermore, the peak value of $\rho_{\mathrm{SH-THE}}$ for W/TmIG reaches 9 nΩ cm, as compared to 6 nΩ cm for Pt/TmIG—a 50% increase. The field region of W/TmIG is also wider than that of Pt/TmIG. For the Pt(3 nm)/Au(1 nm)/TmIG(2 nm) trilayer (Fig. 4c), the phase diagram is very similar to Pt/TmIG (see Fig. 4a) albeit a slight increase in the temperature region to 330-420 K. Additionally, $\rho_{\mathrm{SH-THE}}$ peaks around 6 nΩ cm for the Pt/Au/TmIG trilayer which is close to that of the Pt/TmIG bilayer. Figure 4d shows that the Pt(3 nm)/Ti(1 nm)/TmIG(2 nm) trilayer exhibits no SH-THE for the whole *H*-*T* region.

Lastly, for each temperature measured, we determine $H_{\mathrm{SH-THE,max}}$, the magnetic field at which $\rho_{\mathrm{SH-THE}}$ reaches the maximum for the W/TmIG and Pt/TmIG bilayers as well as the Pt/Au/TmIG trilayer as shown in Fig. 5. While the temperature range varies for each sample, all three exhibit the similar temperature dependence: $H_{\mathrm{SH-THE,max}}$ increases rapidly with T before the SH-THE signal disappears. We fit the $H_{\mathrm{SH-THE,max}}$ vs. T data for each sample to an exponential function, $H_{\mathrm{SH-THE,max}} = a + be^{-E/(k_B T)}$, where a, b, and E are fitting parameters. E represents a characteristic energy that determines the temperature window for the emergence of THE, which is obtained from the fitting to be 0.31 ± 0.01, 0.45 ± 0.01, and 0.54 ± 0.02 eV for the W/TmIG, Pt/TmIG, and Pt/Au/TmIG, respectively. This systematic, exponential temperature dependence possibly originates from the magnetic anisotropy, interfacial DMI, and exchange stiffness,[11, 24, 25] which is not currently understood and requires further experimental and

theoretical investigations.

In conclusion, we investigate the topological Hall effect, which is an indication of topological spin textures, in insulating $Tm_3Fe_5O_{12}$ epitaxial thin films capped with various metals. The presence of the spin-Hall anomalous Hall effect and/or spin-Hall topological Hall effect in these structures reveals the ability of the metal layers to induce interfacial DMI, generate spin accumulation, and detect the magnetization in $Tm_3Fe_5O_{12}$. Our results further clarify the mechanism for electrical detection of topological spin textures in insulating magnetic films.

This work was primarily supported by DARPA under Grant No. D18AP00008. Partial support was provided by the Center for Emergent Materials, an NSF-funded MRSEC, under Grant No. DMR-1420451 for the growth of TmIG films.

References:

1. X. Z. Yu, N. Kanazawa, W. Z. Zhang, T. Nagai, T. Hara, K. Kimoto, Y. Matsui, Y. Onose and Y. Tokura, "Skyrmion flow near room temperature in an ultralow current density," *Nat. Commun.* **3**, 988 (2012).
2. U. K. Rossler, A. N. Bogdanov and C. Pfleiderer, "Spontaneous skyrmion ground states in magnetic metals," *Nature* **442**, 797 (2006).
3. A. Neubauer, C. Pfleiderer, B. Binz, A. Rosch, R. Ritz, P. G. Niklowitz and P. Boni, "Topological Hall Effect in the A Phase of MnSi," *Phys. Rev. Lett.* **102**, 186602 (2009).
4. F. Jonietz, S. Muhlbauer, C. Pfleiderer, A. Neubauer, W. Munzer, A. Bauer, T. Adams, R. Georgii, P. Boni, R. A. Duine, K. Everschor, M. Garst and A. Rosch, "Spin Transfer Torques in MnSi at Ultralow Current Densities," *Science* **330**, 1648-1651 (2010).
5. O. Boulle, J. Vogel, H. X. Yang, S. Pizzini, D. de Souza Chaves, A. Locatelli, T. O. Menteş, A. Sala, L. D. Buda-Prejbeanu, O. Klein, M. Belmeguenai, Y. Roussigné, A. Stashkevich, S. M. Chérif, L. Aballe, M. Foerster, M. Chshiev, S. Auffret, I. M. Miron and G. Gaudin, "Room-temperature chiral magnetic skyrmions in ultrathin magnetic nanostructures," *Nat. Nanotechnol.* **11**, 449-454 (2016).
6. W. J. Jiang, P. Upadhyaya, W. Zhang, G. Q. Yu, M. B. Jungfleisch, F. Y. Fradin, J. E. Pearson, Y. Tserkovnyak, K. L. Wang, O. Heinonen, S. G. E. te Velthuis and A. Hoffmann, "Blowing magnetic skyrmion bubbles," *Science* **349**, 283-286 (2015).
7. C. Moreau-Luchaire, C. Moutafis, N. Reyren, J. Sampaio, C. A. F. Vaz, N. Van Horne, K. Bouzehouane, K. Garcia, C. Deranlot, P. Warnicke, P. Wohlhuter, J. M. George, M. Weigand, J. Raabe, V. Cros and A. Fert, "Additive interfacial chiral interaction in multilayers for stabilization of small individual skyrmions at room temperature," *Nat. Nanotechnol.* **11**, 444-448 (2016).
8. S. H. Woo, K. Litzius, B. Krüger, M.-Y. Im, L. Caretta, K. Richter, M. Mann, A. Krone, R. M. Reeve, M. Weigand, P. Agrawal, I. Lemesh, M.-A. Mawass, P. Fischer, M. Kläui and G. S. D. Beach, "Observation of room-temperature magnetic skyrmions and their current-driven dynamics in ultrathin metallic ferromagnets," *Nat. Mater.* **15**, 501-506 (2016).
9. K.-Y. Meng, A. S. Ahmed, M. Baćani, A.-O. Mandru, X. Zhao, N. Bagués, B. D. Esser, J. Flores, D. W. McComb, H. J. Hug and F. Y. Yang, "Observation of Nanoscale Skyrmions in $SrIrO_3$/$SrRuO_3$ Bilayers," *Nano Letters* **19**, 3169-3175 (2019).
10. J. Matsuno, N. Ogawa, K. Yasuda, F. Kagawa, W. Koshibae, N. Nagaosa, Y. Tokura and M. Kawasaki, "Interface-driven topological Hall effect in $SrRuO_3$-$SrIrO_3$ bilayer," *Sci. Adv.* **2**, e1600304 (2016).
11. Q. M. Shao, Y. W. Liu, G. Q. Yu, S. K. Kim, X. Y. Che, C. Tang, Q. L. He, Y. Tserkovnyak, J. Shi and K. L. Wang, "Topological Hall effect at above room temperature in heterostructures composed of a magnetic insulator and a heavy metal," *Nat. Electronics* **2**, 182 (2019).
12. A. S. Ahmed, A. J. Lee, N. Bagués, B. A. McCullian, A. M. A. Thabt, A. Perrine, J. R. Rowland, M. Randeria, P. C. Hammel, D. W. McComb and F. Y. Yang, "Spin-Hall Topological Hall Effect in Highly Tunable Pt/Ferrimagnetic-Insulator Bilayers," *Nano Letters* **19**, 5683 (2019).
13. H. Nakayama, M. Althammer, Y. T. Chen, K. Uchida, Y. Kajiwara, D. Kikuchi, T. Ohtani, S. Geprags, M. Opel, S. Takahashi, R. Gross, G. E. W. Bauer, S. T. B. Goennenwein and E. Saitoh, "Spin Hall Magnetoresistance Induced by a Nonequilibrium Proximity Effect," *Phys. Rev. Lett.* **110**, 206601 (2013).

14. C. O. Avci, A. Quindeau, C. F. Pai, M. Mann, L. Caretta, A. S. Tang, M. C. Onbasli, C. A. Ross and G. S. D. Beach, "Current-induced switching in a magnetic insulator," *Nat. Mater.* **16**, 309 (2017).
15. H. C. Wang, J. L. Chen, T. Liu, J. Y. Zhang, K. Baumgaertl, C. Y. Guo, Y. H. Li, C. P. Liu, P. Che, S. Tu, S. Liu, P. Gao, X. F. Han, D. P. Yu, M. Z. Wu, D. Grundler and H. M. Yu, "Chiral Spin-Wave Velocities Induced by All-Garnet Interfacial Dzyaloshinskii-Moriya Interaction in Ultrathin Yttrium Iron Garnet Films," *Phys. Rev. Lett.* **124**, 027203 (2020).
16. C. O. Avci, E. Rosenberg, L. Caretta, F. Büttner, M. Mann, C. Marcus, D. Bono, C. A. Ross and G. S. D. Beach, "Interface-driven chiral magnetism and current-driven domain walls in insulating magnetic garnets," *Nat. Nanotechnol.* **14**, 561 (2019).
17. S. Vélez, J. Schaab, M. S. Wörnle, M. Müller, E. Gradauskaite, P. Welter, C. Gutgsell, C. Nistor, C. L. Degen, M. Trassin, M. Fiebig and P. Gambardella, "High-speed domain wall racetracks in a magnetic insulator," *Nat. Commun.* **10**, 4750 (2019).
18. F. Y. Yang and P. C. Hammel, "Topical review: FMR-Driven Spin Pumping in $Y_3Fe_5O_{12}$-Based Structures," *J. Phys. D: Appl. Phys.* **51**, 253001 (2018).
19. H. L. Wang, C. H. Du, Y. Pu, R. Adur, P. C. Hammel and F. Y. Yang, "Scaling of Spin Hall Angle in 3d, 4d, and 5d Metals from $Y_3Fe_5O_{12}$/Metal Spin Pumping," *Phys. Rev. Lett.* **112**, 197201 (2014).
20. C. Hahn, G. de Loubens, O. Klein, M. Viret, V. V. Naletov and J. Ben Youssef, "Comparative measurements of inverse spin Hall effects and magnetoresistance in YIG/Pt and YIG/Ta," *Phys. Rev. B* **87**, 174417 (2013).
21. M. Isasa, E. Villamor, L. E. Hueso, M. Gradhand and F. Casanova, "Temperature dependence of spin diffusion length and spin Hall angle in Au and Pt," *Phys. Rev. B* **91**, 024402 (2015).
22. J. T. Brangham, K. Y. Meng, A. S. Yang, J. C. Gallagher, B. D. Esser, S. P. White, S. S. Yu, D. W. McComb, P. C. Hammel and F. Y. Yang, "Thickness dependence of spin Hall angle of Au grown on $Y_3Fe_5O_{12}$ epitaxial films," *Phys. Rev. B* **94**, 054418 (2016).
23. C. H. Du, H. L. Wang, F. Y. Yang and P. C. Hammel, "Systematic variation of spin-orbit coupling with d-orbital filling: surprisingly large inverse spin Hall effect in 3d transition metals," *Phys. Rev. B* **90**, 140407(R) (2014).
24. S. Schlotter, P. Agrawal and G. S. D. Beach, "Temperature dependence of the Dzyaloshinskii-Moriya interaction in Pt/Co/Cu thin film heterostructures," *Appl. Phys. Lett.* **113**, 092402 (2018).
25. R. Moreno, R. F. L. Evans, S. Khmelevskyi, M. C. Muñoz, R. W. Chantrell and O. Chubykalo-Fesenko, "Temperature-dependent exchange stiffness and domain wall width in Co," *Phys. Rev. B* **94**, 104433 (2016).

Figure Captions:

Figure 1. Structural characterization of metal/TmIG structures. (a**)** Cross-sectional STEM image of a Pt/TmIG(1.85 nm) bilayer on sGGG(111) viewed along the $[11\bar{2}]$ direction. (b) STEM image combined with an EDX color map that distinguishes Tm in the TmIG film from Ga in the sGGG substrate. (c) AFM image of a Ta/TmIG(2 nm) bilayer on sGGG(111) with a roughness of 0.29 nm. (d) An optical microscope image of a Hall bar combined with a schematic to show the geometry of the applied field (H), current (I), and measured Hall voltage (V_{xy}).

Figure 2. Hall measurements of bilayers. Hall resistivity of heavy-metal/TmIG bilayers with (a) Pt, (b) W, (c) Ta, and (d) Au. Prominent peaks are observed for (a) Pt and (b) W on TmIG, indicating the detection of the SH-THE arising from the topological spin textures. (c) Only the SH-AHE and OHE are present for the Ta/TmIG bilayer. (d) Only the OHE is present for the Au/TmIG bilayer.

Figure 3. Hall measurements of trilayers. (a) OHE-subtracted Hall resistivity and (b) SH-THE resistivity of a Pt(3 nm)/Au(1 nm)/TmIG(2 nm) trilayer with a heavy metal (Au) spacer layer showing large SH-THE peaks. OHE-subtracted Hall resistivity of (c) a Pt(3 nm)/Ti(1 nm)/TmIG(2 nm) trilayer with a Ti spacer layer and (d) a Pt(3 nm)/Ta(1 nm)/TmIG(2 nm) trilayer showing only the SH-AHE features.

Figure 4. Spin-Hall topological Hall effect phase diagrams. Magnetic field versus temperature phase diagrams of spin Hall-topological Hall resistivity for (a) a Pt(3 nm)/TmIG(2 nm) bilayer, (b) a W(2 nm)/TmIG(2 nm) bilayer, (c) a Pt(3 nm)/Au(1 nm)/TmIG(2 nm) trilayer, and (d) a Pt(3 nm)/Ti(1 nm)/TmIG(2 nm) trilayer.

Figure 5. Plots of $H_{\mathrm{SH-THE,max}}$ versus temperature for the W(2 nm)/TmIG(2 nm) and Pt(3 nm)/TmIG(2 nm) bilayers as well as the Pt(3 nm)/Au(1 nm)/TmIG(2 nm) trilayer, where $H_{\mathrm{SH-THE,max}}$ is the magnetic field at which $\rho_{\mathrm{SH-THE}}$ reaches the maximum as indicated in the inset. Each set of data is fit to an exponential function, $H_{\mathrm{SH-THE,max}} = a + be^{-E/(k_B T)}$, with R > 0.999.

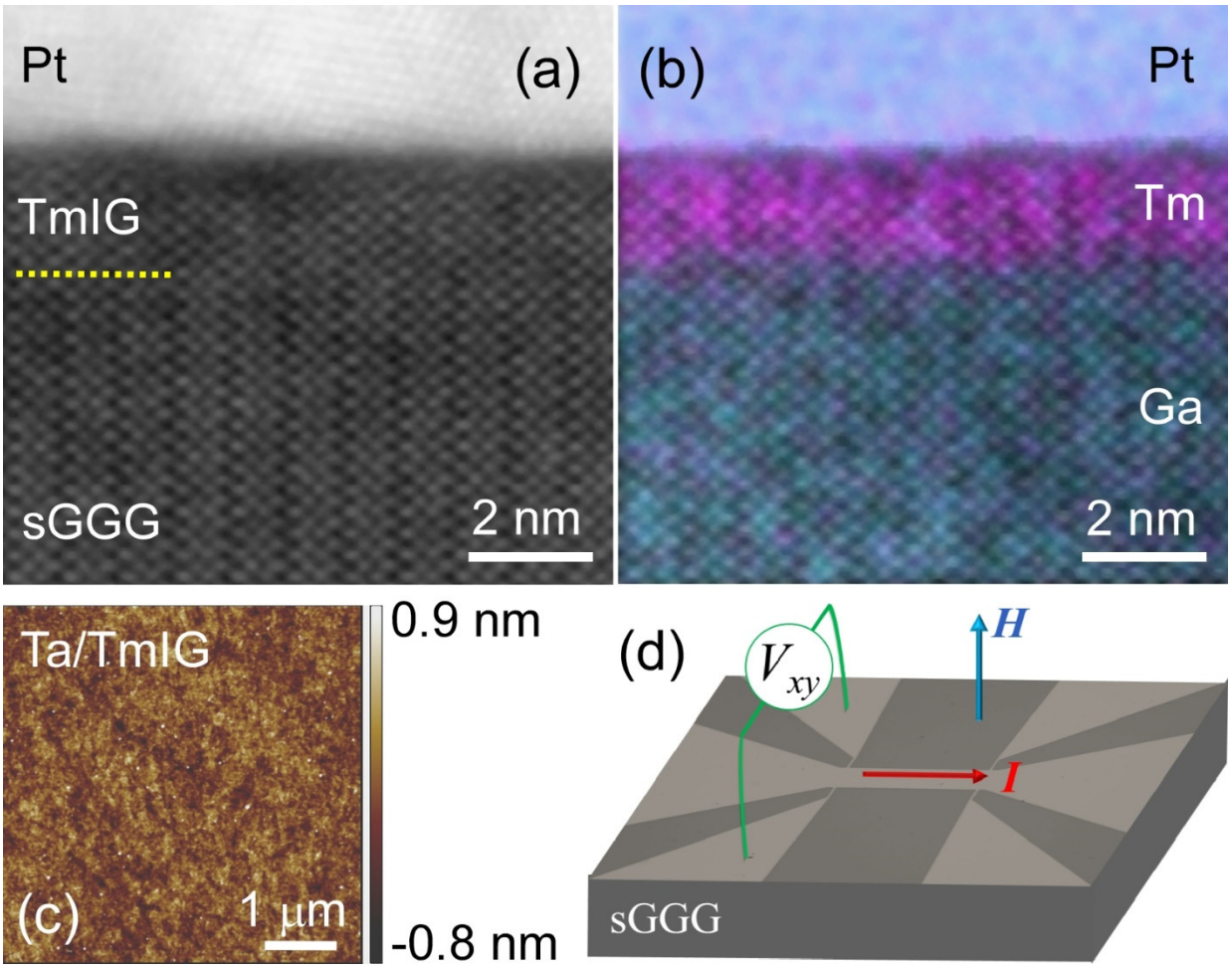
Pt
(a)
TmIG
sGGG
2 nm
(b)
Pt
Tm
Ga
2 nm
Ta/TmIG
(c)
1 μm
0.9 nm
-0.8 nm
(d)
V_{xy}
H
I
sGGG

Figure 1.

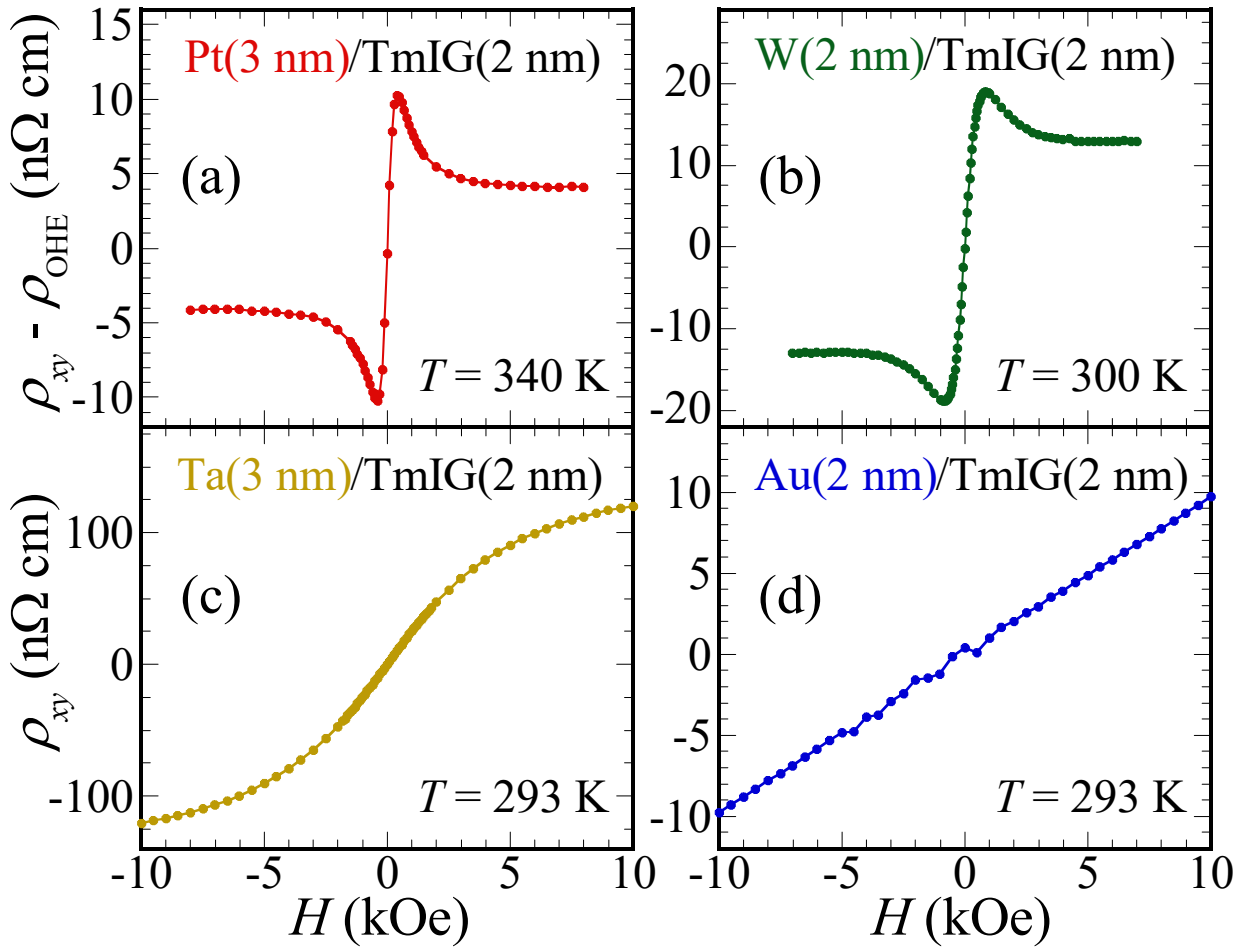
Pt(3 nm)/TmIG(2 nm)
(a)
T = 340 K
W(2 nm)/TmIG(2 nm)
(b)
T = 300 K
Ta(3 nm)/TmIG(2 nm)
(c)
T = 293 K
Au(2 nm)/TmIG(2 nm)
(d)
T = 293 K
ρxy - ρOHE (nΩ cm)
ρxy (nΩ cm)
H (kOe)
H (kOe)

Figure 2.

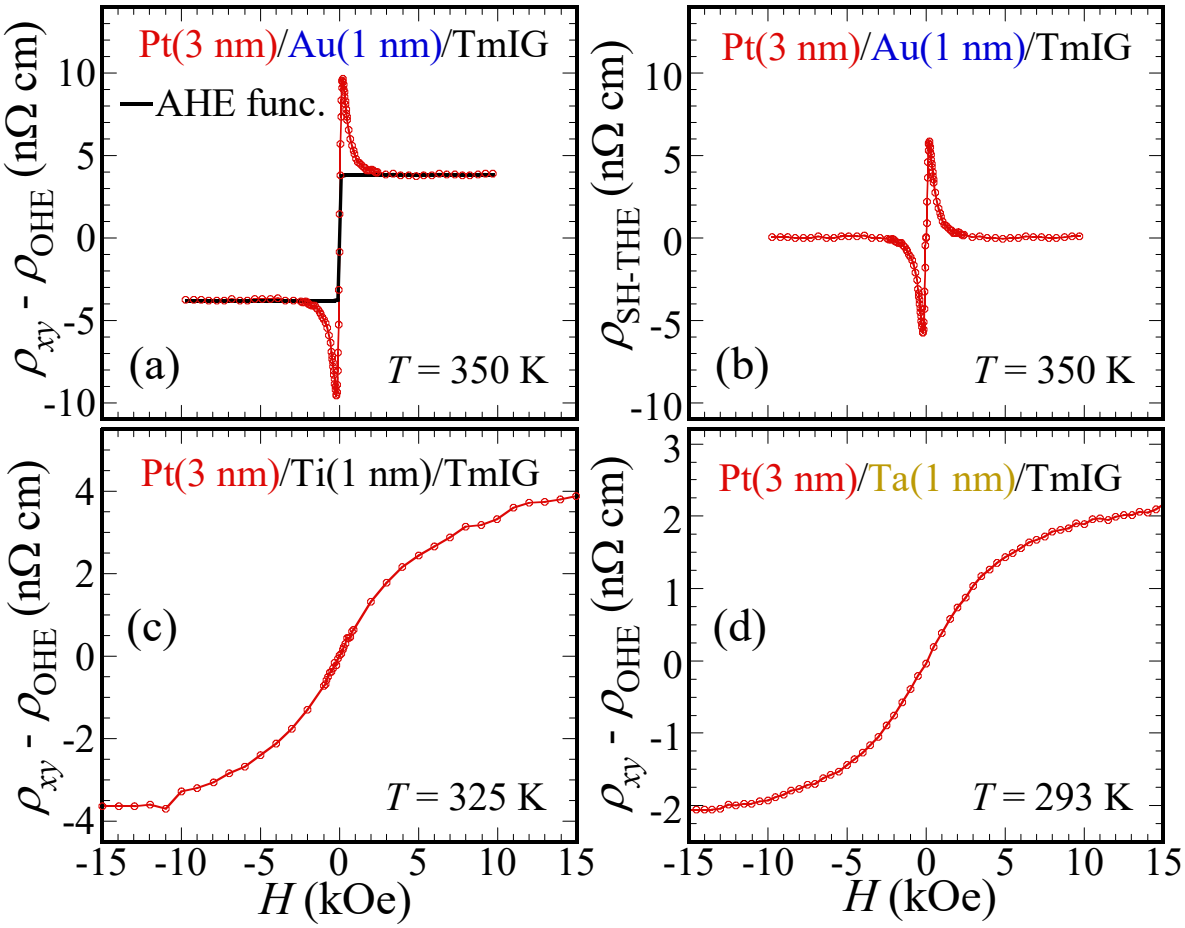
Pt(3 nm)/Au(1 nm)/TmIG
AHE func.
(a)
T = 350 K
ρxy - ρOHE (nΩ cm)
Pt(3 nm)/Au(1 nm)/TmIG
(b)
T = 350 K
ρSH-THE (nΩ cm)
Pt(3 nm)/Ti(1 nm)/TmIG
(c)
T = 325 K
ρxy - ρOHE (nΩ cm)
H (kOe)
Pt(3 nm)/Ta(1 nm)/TmIG
(d)
T = 293 K
ρxy - ρOHE (nΩ cm)
H (kOe)

Figure 3.

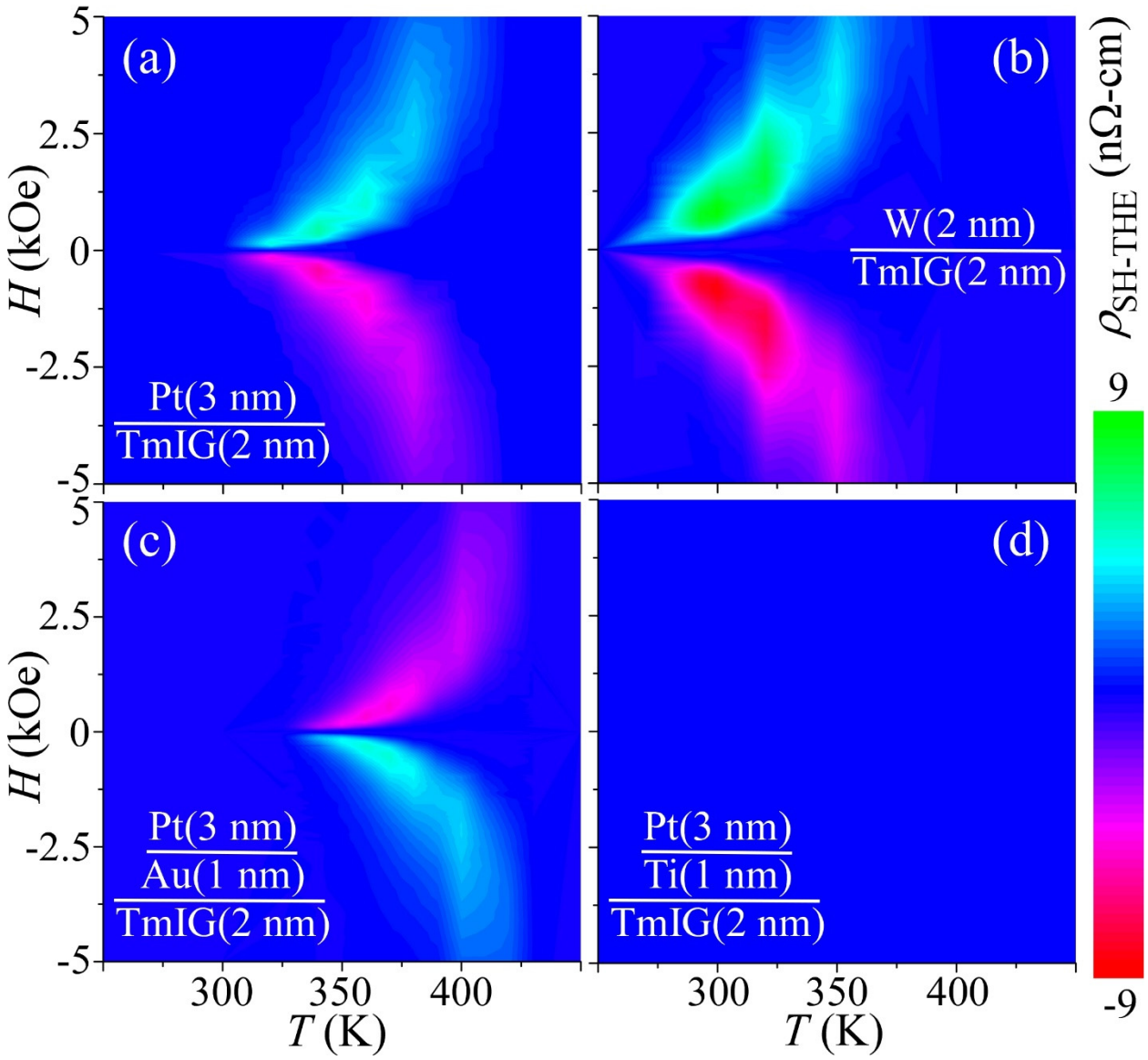
(a)
(b)
(c)
(d)
Pt(3 nm)
TmIG(2 nm)
W(2 nm)
TmIG(2 nm)
Pt(3 nm)
Au(1 nm)
TmIG(2 nm)
Pt(3 nm)
Ti(1 nm)
TmIG(2 nm)
H (kOe)
T (K)
ρSH-THE (nΩ-cm)
5
2.5
0
-2.5
-5
300
350
400
9
-9

Figure 4.

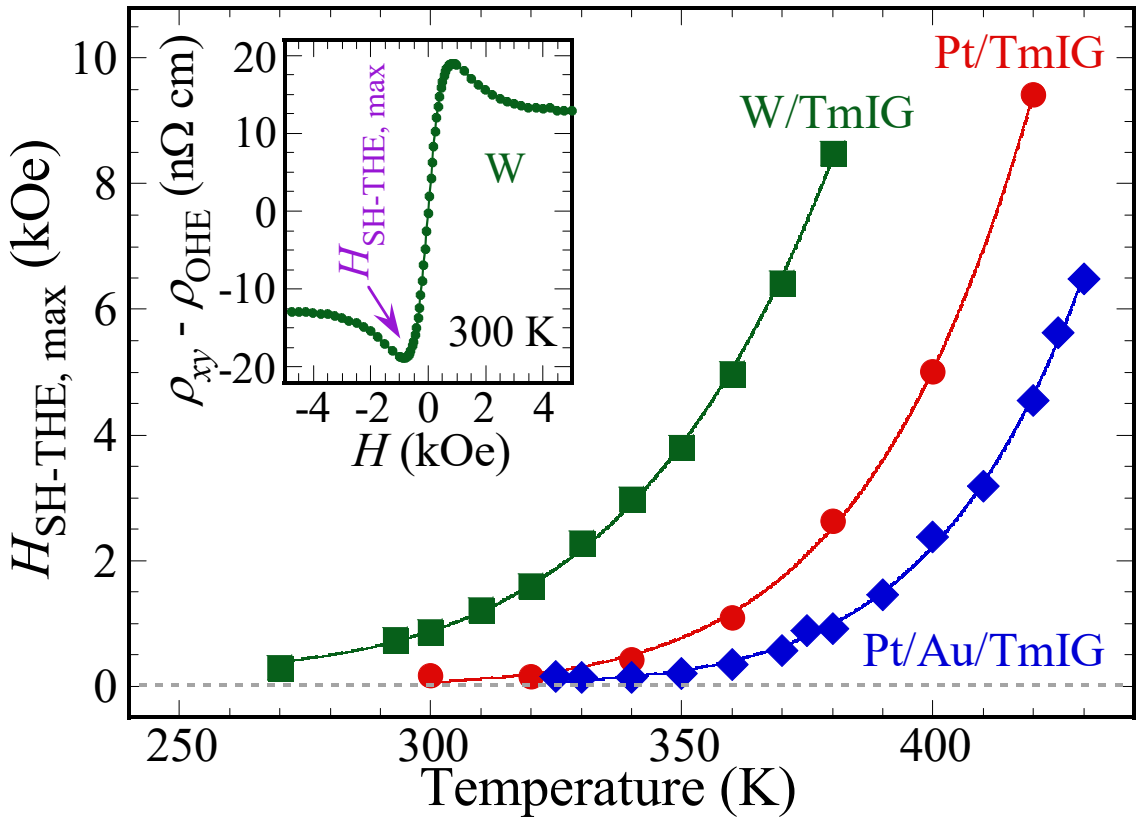
Pt/TmIG
W/TmIG
Pt/Au/TmIG
$H_{SH-THE, max}$ (kOe)
Temperature (K)
250
300
350
400
0
2
4
6
8
10
ρ_{xy} - ρ_{OHE} (nΩ cm)
$H_{SH-THE, max}$
W
300 K
H (kOe)
-4
-2
0
2
4
20
10
0
-10
-20

Figure 5.